Zahn, R., Comas, M.C., and Klaus, A. (Eds.), 1999
Proceedings of the Ocean Drilling Program, Scientific Results, Vol. 161

25. BRITTLE DEFORMATION IN THE METAMORPHIC BASEMENT AT SITE 976: IMPLICATIONS FOR MIDDLE MIOCENE EXTENSIONAL TECTONICS IN THE WESTERN ALBORAN BASIN[1]

M.C. Comas[2] and J.I. Soto[2]

ABSTRACT

During Ocean Drilling Program Leg 161, the basement of the Western Alboran Basin at Site 976 was drilled. Holes 976B and 976E penetrated high-grade metamorphic rocks intersected by polymictic breccia and fault-gouge intervals. Breccia lithotypes and fabrics indicate that the brittle deformation in the basement was mainly from fault-related cataclasis. Neptunian dikes on top of the brecciated basement prove that dilation and brittle tensional fracturing of the basement occurred by the late Serravallian in a submarine environment. Extensive internal microfaulting in breccia porphyroclasts (splintered grains) was related to rapid decompression and exhumation of the metamorphic basement before cataclasis. Our study suggests that breccias and fault-gouge zones were an important pathway for fluids that produced dolomitization after the brittle deformation. On the basis of a study of seismic images across the basement high, we suggest that Site 976 lies near the top of a former rollover structure and the brittle deformation inside was largely produced by counter faults that developed until the middle Miocene.

INTRODUCTION

The highest priority objective at Site 976 was to penetrate at least 200 m into the predicted metamorphic basement to constrain tectonic evolution and geodynamic hypotheses for the Alboran Basin. Site 976 is located in the Western Alboran Basin about 60 km south of Málaga and 8 km northeast of Deep Sea Drilling Program (DSDP) Site 121, drilled during Leg 13 in 1970 (Fig. 1; Ryan, Hsü, et al., 1973). Site 976 lies on a crustal high believed to have formed during the early-to-middle Miocene rifting, which conforms with the most prominent basement structure in the Alboran Sea basin (Fig. 2).

A total of 343.19 m of high-grade metamorphic rocks was cored in two holes at Site 976. Hole 976B (1108.0 m water depth) reached the top of the basement at 669.73 mbsf and penetrated basement to 928.7 mbsf (total recovery 50.4 m). Hole 976E (1107.6 m water depth) reached metamorphic rock at 652.08 mbsf and terminated at 736.3 mbsf (total recovery 24.74 m). In both holes, the basement consists largely of high-grade metamorphic rocks, encompassing high-grade pelitic schist, pelitic gneiss, marble, and calc-silicate rock, with subordinate intrusions and migmatitic segregation of granite. Numerous intervals of polymictic breccias and clay-rich gouges were found in both holes. A 670-m-thick middle Miocene (upper Serravallian) to Pleistocene sequence of open-marine deposits overlies the metamorphic basement at Site 976 (Shipboard Scientific Party, 1996).

Metamorphic rocks recovered resemble the Alpujarride Complex rocks in the western Betic Cordillera, particularly the high-grade metamorphic Alpujarride Units underneath the Ronda peridotite slab (Shipboard Scientific Party, 1996; Sanchez-Gómez et al., Chap. 23, this volume; Soto et al., Chap. 19, this volume). In that region, the metamorphism gives early Miocene radiometric ages (18–20 Ma; Zeck et al., 1992; Monié et al., 1994).

Basement rocks from Holes 976B and 976E underwent penetrative ductile deformation that produced a series of metamorphic structures and fabrics. The numerous zones of breccia and fault gouges are evidence that subsequent, extensive brittle deformation cross-cut the metamorphic basement (Comas, Zahn, Klaus, et al., 1996).

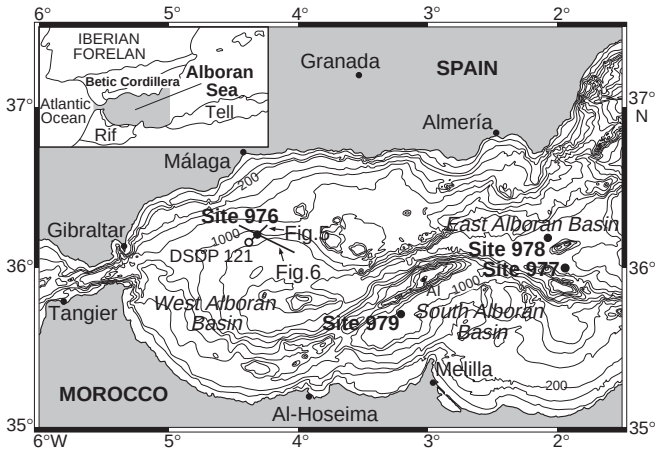

Figure 1. Location of DSDP 121 and ODP Leg 161 Sites in the Alboran Sea. Bathymetry contours in meters, contour interval 200 m. Locations of seismic profiles shown in Figures 5 and 6 are marked. AI = Alborán Island. Inset map: location of the Alboran Sea between the Betic and Rif mountain chains.

This paper describes and interprets the polymictic breccias and gouges cored at Site 976. The main objective of this study was to determine features of the brittle deformation encountered in the basement high and investigate their possible relationship with the middle Miocene extensional tectonics in the Western Alboran Basin. We present and interpret reflection seismic profiles across the basement horst and the Western Alboran Basin in support of our conclusions.

TECTONIC SETTING

The Alboran Basin is generally identified as one of the western Mediterranean basins that originated at the site of a former (Late Cretaceous to Paleogene) collisional orogen. It developed by crustal thinning processes within the Neogene Eurasia-African plate convergence setting. The Alboran Sea basin is located behind an arc-shaped orogenic belt formed by the Betic (southern Spain) and Rif (Morocco) Chains (Fig. 1, inset map).

[1]Zahn, R., Comas, M.C., and Klaus, A. (Eds.), 1999. *Proc. ODP, Sci. Results,* 161: College Station, TX (Ocean Drilling Program).

[2]Instituto Andaluz de Ciencias de la Tierra, CSIC and University of Granada, 18002 Granada, Spain. Comas: mcomas@goliat.ugr.es

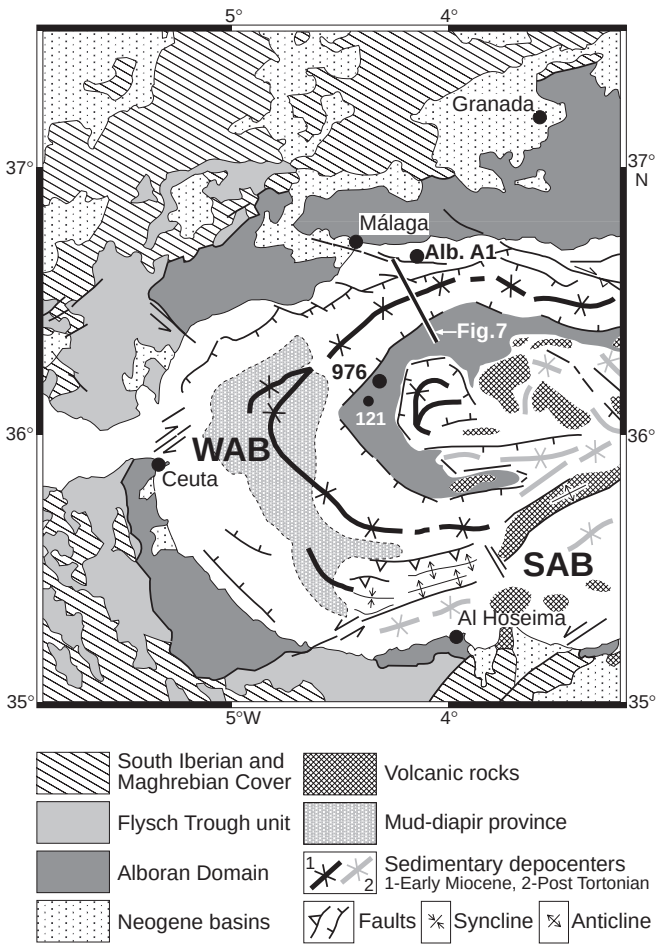

Figure 2. Tectonic map of the Western Alboran Basin showing position of Site 976 on the top of the basement horst. Location of seismic profile shown in Figure 7 is marked. WAB = Western Alboran Basin, SAB = South Alboran Basin.

More than 6 km of lower Miocene (late Aquitanian(?)–Burdigalian) to Pleistocene sediments cover the Alboran Sea basin. In the Betic and Rif Chains, numerous intramountain depressions, or "Neogene basins," contain Miocene marine sequences, counterparts of those filling the Alboran Sea basin (Fig. 2). These on-land basins are interpreted as corresponding to, or superimposing marine depocenters from, the ancestor early-to-middle Miocene Alboran Basin. Thus, during the Miocene, the Alboran Basin ranged north-south beyond the present limits of the Alboran Sea (Comas et al., 1992; García-Dueñas et al., 1992).

The continental crust thins from 38 km in the Betic Chain to about 15–20 km beneath the central Alboran Sea (Torné and Banda, 1992; Banda et al., 1993; and references therein). Heat-flow data suggest an eastward decrease in lithospheric thickness from 60–90 km in the Western Alboran Basin to about 35–40 km and concurrent crustal thinning from 14–16 km to 10–12 km in the transition from the East Alboran Basin to the South Balearic Sea (Polyak et al., 1996).

The basement of the Alboran Basin is formed primarily of metamorphic complexes belonging to the Alboran Crustal Domain (the internal complexes of both the Betic and Rif Chains); composed of a syn- and postmetamorphic pre-Miocene polyphase thrust-stack that includes three nappe complexes: the Nevado-Filabride, Alpujarride, and Malaguide. Site 976 data confirmed that the Alboran Domain has north-south continuity beneath the Alboran Sea (Comas, Zahn, Klaus, et al., 1996). East of the 4°W meridian, most of the basement highs appear to consist of volcanic edifices, as revealed by dredging (Gierman et al. 1968) and diving data (Comas et al., unpubl. data). Notwithstanding, the nature of the absolute basement in the eastern region is unknown.

The Alboran Sea basin (Fig. 2) was structured by superimposed extensional and contractional tectonics. Late orogenic rifting and progressive exhumation of the Alboran Domain took place from at least the early Miocene to the early Tortonian (Comas et al, 1992; Watts et al., 1993; Comas et al., 1995). In the outcropping Alboran Domain, large-scale extensional detachment systems are superimposed on the continental collisional structures (García-Dueñas et al., 1992; Crespo-Blanc et al., 1994; Martínez-Martínez and Azañon, 1997; Balanyá et al. 1997; and references therein). Results from metamorphic rocks sampled at Site 976 indicate that Miocene crustal extension was accompanied by rapid tectonic exhumation of middle crustal rocks and advection of heat at relatively low pressure (Comas, Zahn, Klaus, et al., 1996; Platt et al., 1996; Soto et al., Chap. 19, this volume). Extensional processes produced early Miocene and late Serravallian/Tortonian alkaline and calc-alkaline magmatism (Bellon et al., 1983; Hernández et al., 1987), as well as the notable mud diapirism in the Western Alboran Basin (Fig. 2). On-shore and offshore data indicate that the main rifting ceased by the late Tortonian. After that, contractive tectonics disjointed the Alboran Basin into sub-basins, separated by emerged or submarine highs. These tectonics produced a north-south shortening and considerable east-west elongation of the whole area (Betic and Rif Chains and Alboran Basin). East-west and east-northeast–west-southwest trends of folds and approximately northwest and northeast conjugate strike-slip fault systems are apparent from seismic lines in the Alboran Sea basin (Fig. 2). Pliocene–Pleistocene tectonics were largely responsible for the present-day seafloor physiography and location of the present coastline (Comas et al., 1992).

METHODS

Macroscopic observations on cores and on large slab samples were made during the cruise and the postcruise sampling meeting at the Bremen Ocean Drilling Program (ODP) Repository. Analysis of logging data was an important tool in interpreting breccia intervals with poor recovery. Forty-eight thin and polished sections of cemented breccias were prepared and examined petrographically to identify types of clasts, matrix, mineral composition, and fabrics. For selected samples, staining methods (Alizarin-Red S) and cathodoluminescence observations (CL) were performed. X-ray fluorescence analysis gave information on chemical compositions of breccia matrix.

OCCURRENCE OF BRECCIAS AND GOUGES

Intervals of breccia and clay-rich gouges in Holes 976B and 976E mark zones of brittle deformation. Their widespread occurrence largely determined the low total recovery at Site 976 (Fig. 3). In both holes, late Serravallian (Zone NN7, about 11–12 Ma) deposits overlie the brecciated basement (lithostratigraphic Unit IV; Shipboard Scientific Party, 1996)

On the mesoscopic scale, breccias correspond to a cemented or weakly cemented polymictic breccia formed of high-angular and variable grain-sized clasts of nearby basement metamorphic lithologies, which made up >50% of the whole rock (Pl. 1, figs. 1, 2, 4, 6). Fabrics present in breccias are similar on both mesoscopic and microscopic scale, and shown a porphyroclastic texture where clasts (porphyroclasts) and particle-sized grains range from about 7 cm to mi-

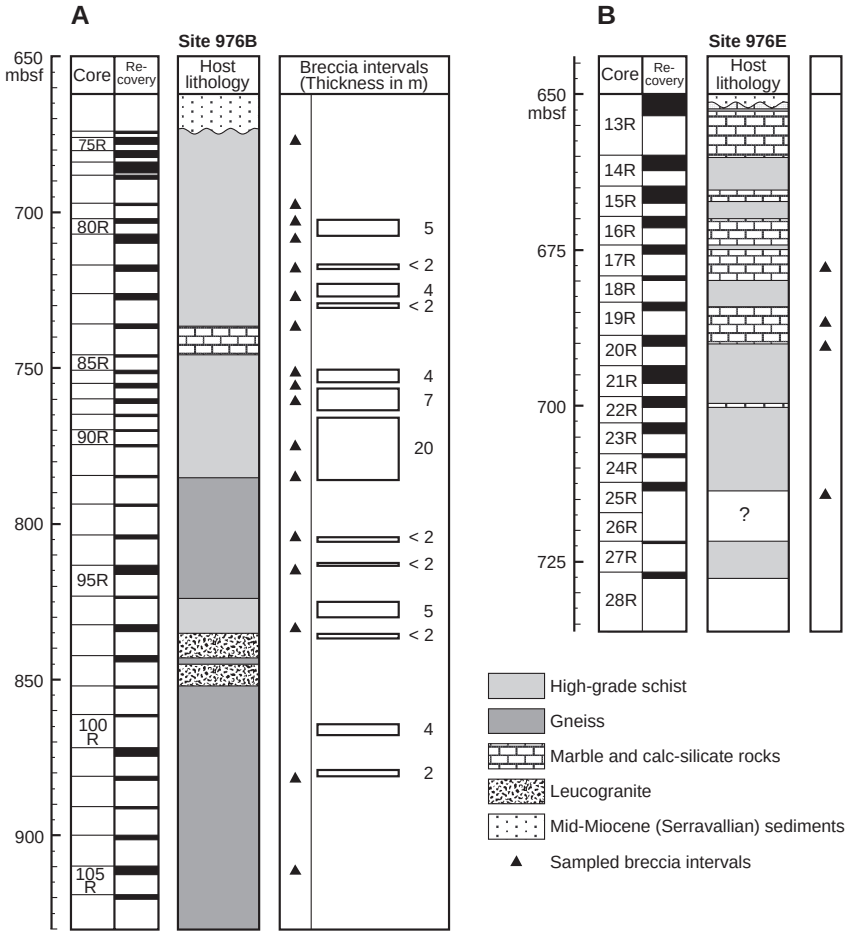

Figure 3. Occurrence of breccias and fault gouges within the metamorphic basement at Site 976. **A.** Breccia intervals drilled in Hole 976B. Thickness of breccia intervals deduced from logging data. **B.** Breccia intervals drilled in Hole 976E.

croscopic. The breccias usually have a fine-grained matrix, formed by comminution and alteration of metamorphic rocks and a carbonate-rich "cement." Gouges are dark-colored, uncemented, or poorly cohesive rocks with a clay-rich groundmass or matrix and scattered angular porphyroclasts (<50%) of similar lithologies as in breccias. More cohesive gouges usually contain cataclastic foliation structures at mesoscopic scale (Pl. 1, fig. 3).

The uppermost breccia interval drilled at Hole 976B (Sections 161-976B-74X-1, through 75R-2; Pl. 1, fig. 1, fig. 2) is a coherent cemented breccia with angular to subrounded clasts of variable grain size (0.1–60 mm), formed of high-grade schist (>70%), quartzite (<25%), and minor grayish fine-grained marble (<5%). The matrix is dolomitic silty claystone, containing foraminifer ghosts, with frequent scattered biotite flakes and occasional single garnet crystals (<15%), including dolomite, calcite, ankerite, siderite, quartz, and clay minerals (from X-ray diffraction [XRD] data).

Sections 161-976B-79R-1 to 81R-2 correspond to basement rocks with discrete gouge and breccia intervals. Logging data reveal that these intervals extend from 702 to 708 mbsf (Figs. 3, 4). Breccia contains 0.1–10-mm fragments of schist (45%), quartzite (35%), and dolomite marble (20%) in a yellow dolomitic or clayey matrix. There is some evidence of oxidation, dissolution, and alteration in porphyroclasts and matrix as shown by abundant clay and oxide stains in pelitic fragments and solution cavities in dolomite fragments. Gouge occurs with up to 8 mm scattered porphyroclasts of high-grade schist and dolomite marble, and a clayey groundmass formed of ankerite, kaolinite, siderite, and quartz (XRD data).

Logging data suggest the occurrence of nonrecovered breccia or gouge intervals at 716–720 and 722–726 mbsf, which probably determined the low recovery from Cores 161-976B-81R and 82R (26% in both cases). Logging at these intervals is characterized by low resistivity, gamma-ray (≈25 API), natural radioactivity, and photoelectric factor (≈1 Ωm) values.

An intensely fractured interval occurs through Cores 161-976B-86R to 88R (750–785 mbsf; Fig. 4). This interval (20–25 m thick) has abundant, poorly consolidated or cohesive clayey gouges (Shipboard Scientific Party, 1996). It most likely corresponds to a thick fracture zone, wherein we have distinguished several discrete brecciated zones, at 750–754, 758–765, and 767–785 mbsf (Fig. 4), corresponding to Sections 161-976B-86R-1 through 92R-1.

Gouges from this interval are polymictic, matrix-supported, poorly cemented rocks with variably-sized angular porphyroclasts. Porphyroclasts consist of biotite-rich schist and foliated gneiss (60%–70%, 1–60 mm); angular, white quartzite grains (20%–25%, up to 30 mm); and rounded and banded marble fragments (5%–20%, up to 40 mm). The silt-sized groundmass is formed of dolomite, calcite, kaolinite, and siderite, with minor biotite and quartz (XRD data). Logging data reveal a relatively consolidated (regular resistivity = <10 Ωm) and dark zone (photoelectric factor = <3 barn/e^-), with high gamma-ray values (≈70–75 API; Fig. 4). Geochemical profile done by logging along this interval shows a sharp increase in the concentration of Cl, Fe, and Si, which suggests extensive mobilization of these elements along the fracture zone. Representative macroscopic textures and structures in this fracture zone include multistage brecciation, crushed clasts (porphyroclasts), incipient cataclastic foliation surrounding crushed clasts, with occasional asymmetric fish-tails, and the presence of minor-scale fault planes with slickensides and ridge-in-groove lineations (Shipboard Scientific Party, 1996).

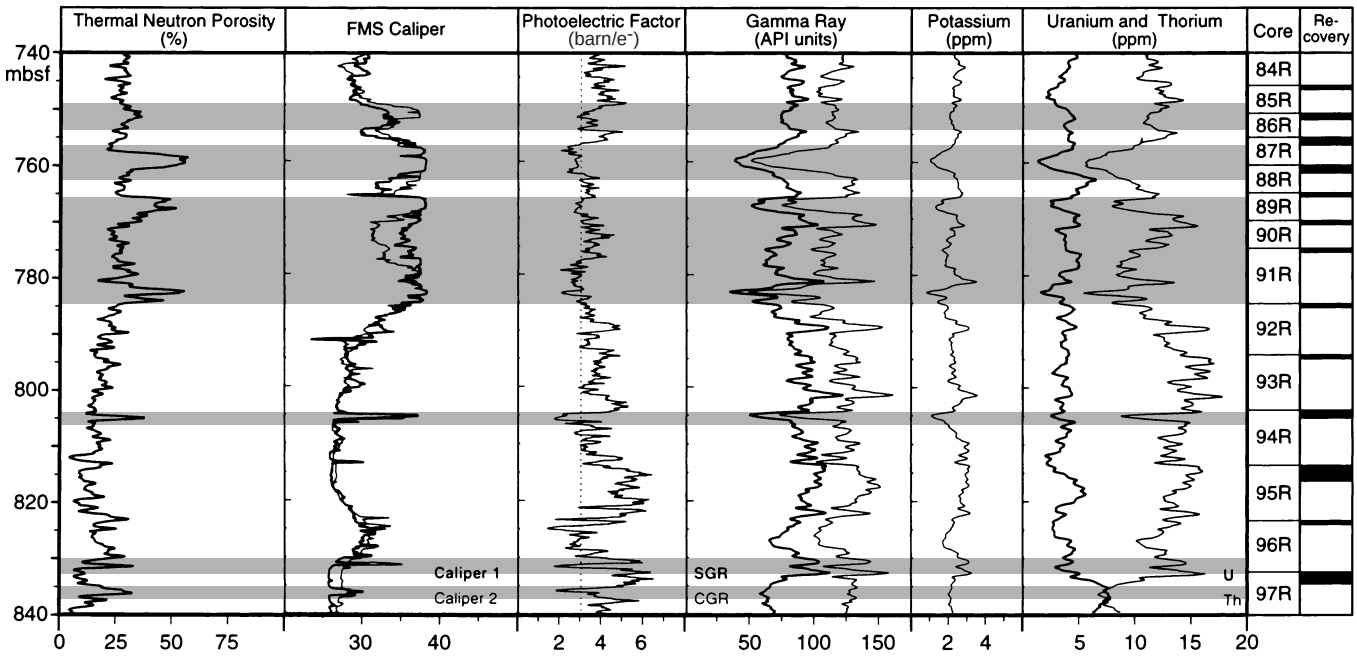

Figure 4. Logging expression of selected breccia and fault-gouge intervals drilled in Hole 976B. Shaded bands correspond to main intervals of brittle deformation.

The lower 145 m of the basement section (from 785 to 930 mbsf) at Hole 976B has narrower (<5 m thick) breccia and gouge zones (Pl. 1, fig. 3), with similar lithologic and logging characteristics.

The brecciated intervals at Hole 976E (Pl. 1, figs. 4–6) have similar characteristics to those described in Hole 976B. Nevertheless, in Hole 976E breccia intervals are thinner (<150 cm) and dolomite-cemented marble breccia is more abundant. Marble breccia has angular clasts of calcitic or dolomitic marble (<40 mm long, up to 90%), biotite-rich high-grade schist (10%–40%), calc-silicate rocks, and minor quartzite (<10%) (Pl. 1, fig. 4). The matrix (size-grain fraction <2 mm) has abundant, finely comminuted biotite flakes. Matrix mineral components are dolomite with minor ankerite, quartz, and biotite (XRD data). The abundance of marble and calc-silicate rocks interlayered in the uppermost 40 m of the basement sequence (up to 690 mbsf; Fig. 3B), seems to account for the widespread occurrence of marble breccias in Hole 976E in contrast with Hole 976B.

The upper 75 m of Hole 976E (up to 715 mbsf; Fig. 3B) is also characterized by fine-laminated, particulated material (from sediments or finer comminuted matrix) filling fractures or fissures that cross-cut or follow the main foliation of the metamorphic rocks. Laminations are defined by oriented flakes of biotite and small schist fragments (Pl. 1, fig. 5). In some cases the fissures connect with breccia pocket intervals. The dominant orientation of these fractures is subvertical, with a maximum length of 30–40 cm and 1–15 mm thick.

Cemented Breccias: Petrographic Results

Thin sections of polymictic cemented breccias from basement cores at Site 976 show complex fracturing and fabrics similar to that observed in hand samples. Microscopic features also indicate that breccias formed in situ. Photomicrographs of fabrics from representative breccia samples are shown in Plates 2, 3, and 4.

At Hole 976B, just overlying the brecciated basement sections, sediments consist of uncemented or weakly cemented, coarse-grained, poorly sorted, lithic silty sands and conglomeratic sands with pebbles of metamorphic rocks. In thin sections of cemented sandstones, siliciclastic components of the sand-sized fraction are quartz, biotite, glauconite, and fragments of schist and quartzite. The silt-sized matrix with similar siliciclastic components is cemented by euhedral to subhedral replacive dolomite crystals. The sandstone contains calcareous nannofossils and benthic and pelagic foraminifers (Shipboard Scientific Party, 1996; Pl. 2, figs. 1, 2). In Hole 976E sediments just above the basement breccias consist of nannofossil-rich claystones. Breccias from the uppermost basement cores in Holes 976B and 976E (Cores 161-976B-74X and 75R, and Core 161-976E-16R) have matrixes largely consisting of those sediments that largely percolated into the previously brecciated basement from the overlying late Serravallian sequence (Pl. 2, figs. 3–6).

Microscopically, the breccia clasts appear to have derived from the metamorphic basement, as all clast lithologies in thin sections match those of the metamorphic host rocks. Breccias have high variability in clast and grain size, with fragments ranging from <1 mm to >5 cm in diameter (most are 0.1–4 cm). Large fragments (porphyroclasts) are generally broken with internal cracks cemented by dolomite or filled-up with the matrix.

The breccia fabric grades from grain-supported to clay- or dolomite-rich matrix-supported fabrics with a porphyroclastic texture, including randomly oriented highly angular pebble- to silt-sized clasts of different lithologies, and is characterized by a variety of deformational structures (Pls. 3, 4). Bedding is not apparent in thin sections, but several samples show elongated fragments parallel to the host rock wall (Pl. 4, fig. 1). Vague clusters of smaller fragments, or mica flakes, define laminations in the matrix (Pl. 3, figs. 1, 5). Breccia clasts are unaltered, except within their outer margins, where they show grain dissolution or alteration by replacive dolomite crystals. Breccias are slightly veined or un-veined at microscopic scale.

Fabrics reveal intense cataclastic grain breakage (as much as 80%). Quartzite or quartz grains display internal splint-breakage texture (splintered quartz; Pl. 4, figs. 1–3). Commonly, fragments in lithoclasts or quartz grains can be fitted together, indicating grain dilation and disaggregation with no major rotation between the elements of each original porphyroclast (Pl. 3, figs. 1, 6; Pl. 4, fig. 4). Cathodoluminescence microscopy allows clast correlation to distinguish smaller clastic fragments originating via cataclastic processes and reveals

indications of grain-size reduction by grain breakage (Pl. 3, fig. 6; Pl. 4, fig. 3).

In thin section, the silt-sized matrix or groundmass consists of dark-gray, "clotted" clay and dolomicrite, very fine fragments of schist, fine-grained quartzite, quartz, biotite, chlorite, and sericite. At the uppermost basement cores, foraminifers have been found in the matrix (Pl. 2, figs. 4, 5).

"Cements" largely comprise planar to nonplanar (see Sibley and Gregg, 1987) crystalline replacive dolomite. Replacive dolomite partially to almost completely (up to >90%) replaces the breccia matrix and porphyroclast borders (e.g., quartz, biotite) in many samples (Pl. 2, figs. 3, 4; Pl. 3, figs. 2, 4). Cathodoluminescence observations indicate at least two generations of dolomite growth, as denoted by recrystallization and replacement of former dolomite crystals. Replacive dolomite in breccia matrix display fine (<30 µm) to medium (<70 µm) subhedral to anhedral crystalline texture (Pl. l, figs. 3, 4, 6). More rarely, dimensions in cements are larger than 200 µm; however, isopachous rims of bladed prismatic dolomite bounding clasts, locally changing to a central fill of blocky dolospar coarsening inward, have been noted in some samples (Pl. 3, fig. 4). Dolospar cement fill is not present everywhere, but some samples include saddle-shaped (curved crystal boundaries; Pl. 3, fig. 3) dolosparite. Complex, zoned saddle dolomite cements compose less than 5% of all dolomite cement in the samples studied. Dolomite crystallization produced replacement in quartz, feldspar, and biotite grain surfaces (Pl. 3, figs. 2, 4). Displacive dolomite textures are also common, occurring as bladed- to planar-displacive dolomite crystals filling discrete veins or micro-fractures cross-cutting quartz, quartzite, and biotite grains (Pl. 4, figs. 1, 2, 6). Calcite cement is a minor component in breccia matrix, but it has been observed filling a few thin veins. There is no textural evidence of subaereal cements or weathering alterations in the studied breccias, as pendant or meniscus cements neither calcrete textures have been clearly recognized in thin sections. However, this point deserves to be explored by further geochemical studies.

Matrix composition and textures indicate a relatively broad spectrum of cemented-breccia types in basement cores. Two end-members of this spectrum can be considered as representative lithotypes of these breccias: (1) dolomite-cemented breccia and (2) clay-matrix cataclastic breccia.

1. Dolomite-cemented breccia (Pl. 2, figs. 3, 6; Pl. 3, figs. 2–4) is largely found in the upper core from Hole 976B (Cores 161-976B-74X through 86R) and are common in Hole 976E from Cores 161-976E-16R through 20R. It comprises angular metamorphic-rock clasts (<60%) in fine to medium-crystalline anhedral to subhedral dolomite matrix (>40%) with minor fine-grained quartz. Fragments are floating in a light-colored aggregate of dolomite crystals (dolomicrite) with noncataclastic or minor cataclastic structures or fabrics. Replacive dolomite is volumetrically important in the matrix breccia, indicating that in places dolomitizing fluids were able to fully replace the original matrix.
2. Clay-matrix cataclastic breccia (Pl. 3, figs. 1, 5, 6; Pl. 4) comprises angular metamorphic-rock fragments (>70%) in a dark, heterogeneous matrix (<30%) consisting of clay, mica, and comminuted fragments from larger clasts. Cataclastic fabrics and structures are common in this breccia type. Overprinting of microscopic structures and mineral growth relationships suggest at least two main phases of brittle deformation in these breccias, which yield cataclastic fabrics (B1 and B2 in Pl. 3, fig. 6). Furthermore, we have identified a third stage that resulted in local renewed grain fracture accompanied or followed by late replacive dolomite neo-crystallization. In general, dolomite in this breccia type postdates cataclasis (Pl. 4, fig. 1, fig. 2).

BRITTLE DEFORMATION: FAULTING, BRECCIATION, AND FRACTURING

The thick gouge interval in the basement section at Hole 976B (750–785 mbsf) seems to consist of metric scale, discrete bands of cataclastic rocks with anastomosing geometry. The band of cataclastic rock surround slices of wall rock with minor or no evidence of brittle deformation (Fig. 4), a geometry common to brittle fault zones (e.g., Koestler and Ehrmann, 1991; Sibson, 1996); therefore, we interpret this gouge interval as corresponding to a significant fault zone within the basement. The fault-gouge interval coincides with a major change in basement lithology, which is richer in gneissic rocks downhole (Fig. 3A). This observation, together with the rock types recovered and the brittle structures encountered, suggests that this interval marks a major fault in the basement section. According to the seismic images, we suggest that the fault zone may correspond to a less than 40° westward-dipping brittle fault (Fig. 5). The footwall of this fault is characterized by an increasing downward dip of the reference surfaces (below 710 mbsf the magnetic foliation dips more than 70°). The sense of shear in this fault could not be determined by any of the available drilling data. Formation MicroScanner data at Hole 976B on shallow-dip planes from fractures or foliations below the fault zone show a north-northeast to north-northwest variable trend with a general dip (<30°) towards the west (de Larouzière et al., Chap. 24, this volume).

We consider the majority of the breccia intervals to be cataclasites (sensu Twiss and Moores, 1992), as clear cataclastic structures have been recognized in most breccia samples. Structures include grain disaggregation and fracturing (Pl. 3, figs. 1, 6; Pl. 4, fig. 3), and cataclastic flow, foliation, or lineation (Pl. 1, fig. 3; Pl. 3, figs. 1, 5, 6; Pl. 4, figs. 1–5). Cataclasites are known to form by frictional sliding and fracture processes in different tectonic settings: wrench tectonics (Blenkinsop and Sibson, 1992; Tanaka, 1992), thrusting or nappe-stacking (House and Gray, 1982), and extensional faulting (Malavieille, 1993).

A growing array of geological and geophysical data suggests that the grain-scale deformation mechanism in cataclasites, and the state of stress in active faults are largely controlled by high pore-fluid pressures in the fault zone (e.g., Carter et al., 1990; Wintsch et al., 1995). These pressures are caused by either fluids migrating to and through the faults during their movement or by fluids trapped in fine-grained clay gouge zones (Chester et al., 1985; Byerlee, 1990; Evans, 1990). The presence of fluids favors cataclastic deformation and hydraulic fracture by reducing the effective confining pressure, and cataclastic flows develop through successive cycles of softening-hardening of fault zones (Babaie et al., 1991; Wintsch et al., 1995).

Extensive internal microfracturing (splintered grains) observed in some metamorphic porphyroclasts of the reported samples may have developed by rapid decompression during exhumation of the metamorphic basement produced by extensional faulting. Further cataclastic structures postdate the intragranular microfractures (Pl. 4, figs. 1–3).

There is strong evidence for superficial extension in breccias and metamorphic rocks, thereby creating open spaces within displaced host rocks. In the uppermost basement cores from Holes 976B and 976E (Pl. 1, figs. 2 and 4), fractures have sediment-fill derived from above and are therefore considered neptunian dikes and sills (e.g., Bernoulli and Jenkyns, 1974). Neptunian dikes prove that the dilation and brittle tensional fracturing of the basement at Site 976 occurred in a submarine environment (i.e., by the late Serravallian; Shipboard Scientific Party, 1996). In Hole 976E, sediment injection into open fractures from below are denoted by convex-up laminations in sediment fill, thus suggesting strong fluid circulation between a connected open-fracture closed system in the basement high (Pl. 1, fig. 5).

Sediment injections into open fractures, and pervasive dolomitization, together with the distinctive geochemical composition in cat-

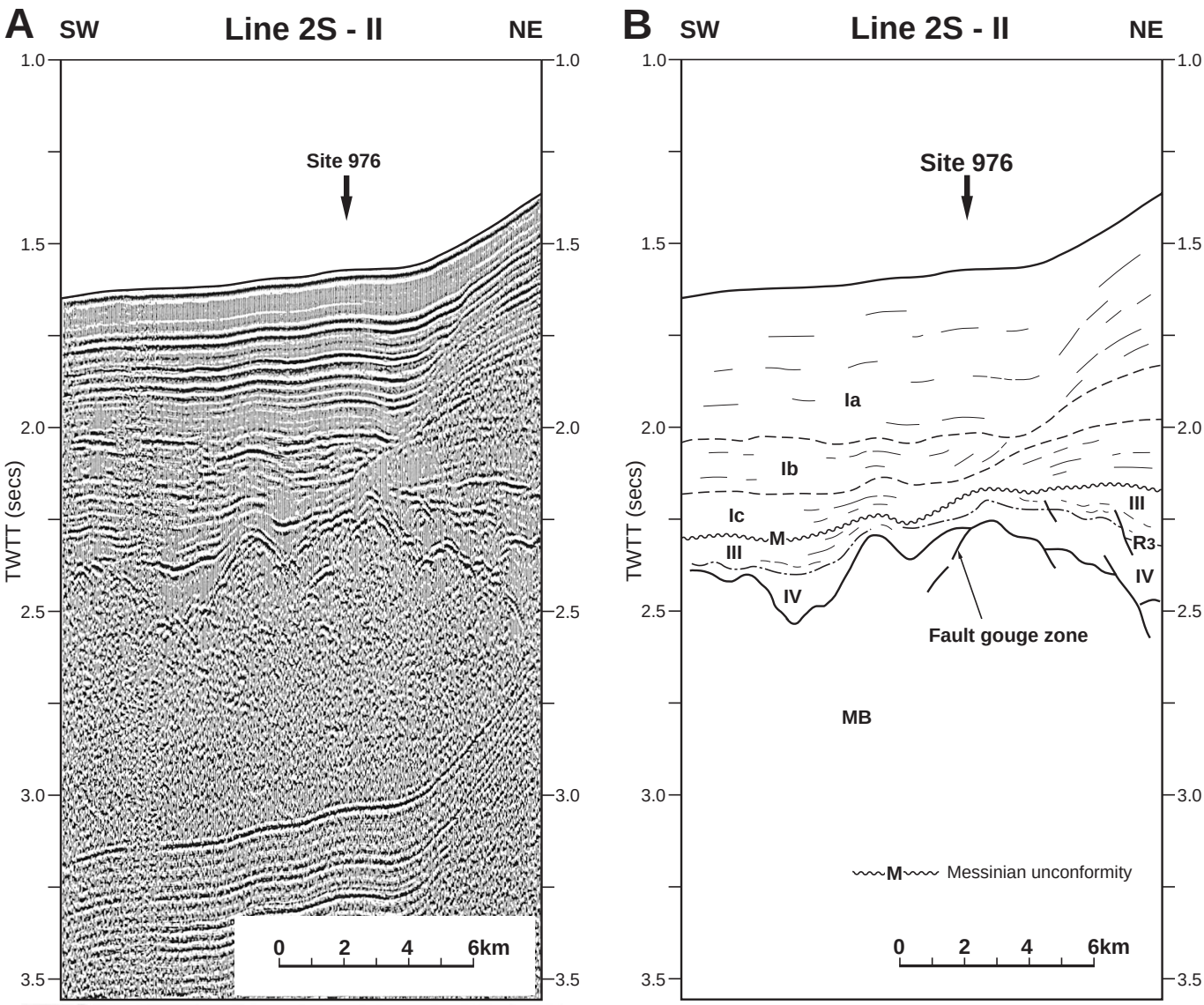

Figure 5. *JOIDES Resolution* seismic Line 2S-II (single channel) across Site 976. **A.** Original profile. **B.** Drawn interpretation of Line 2S-II based on Site 976 data (modified from Shipboard Scientific Party, 1996). Reflectors and lithoseismic units I–IV from Comas et al. (1992). Reflectors correspond to major unconformities within sediments: R3 = early Tortonian, M = Messinian "M" unconformity. Ia = Pleistocene, Ib and Ic = Pliocene sequences (Comas, Zahn, Klaus et al., 1996). MB = Metamorphic basement. Location of seismic line is shown in Figure 1.

aclastic zones, indicate fluid-assisted processes for brittle deformation at Site 976. Coarse-grained saddle dolomite suggests dolomitization by fluids at high temperature, comparable to those in which dolomitization resulted in experimental studies, that is, as low as 100°C (Gaines, 1980; Sibley et al., 1994). Our data reveal that the brecciated basement at Site 976 was an important pathway for fluids, probably including heat advention associated with the tectonic regime. Hydrothermal solutions are potential dolomitizing fluids, at least for replacive nonplanar and saddle dolomite. However, whether fluids correspond to younger or older sea water, somewhat modified by host-rock interaction, or just to hydrothermal brines, they deserve to be investigated by further geochemistry analyses, which is beyond the scope of this paper.

TECTONIC IMPLICATIONS: DISCUSSION

One of the more noteworthy results from studies of Site 976 samples was to prove that extensional tectonics in the Alboran Sea basin continued up until the late middle Miocene and that the structural basement high was exposed to the sea floor by about 12 Ma (late Serravallian; Shipboard Scientific Party, 1996). However, direct drilling gives no further information on the structural behavior of this basement high.

Regional seismic data in the Western Alboran Basin are worth considering to maximize drilling data and better understand the brittle fracturing in the top of the basement high. With this aim, we discuss below seismic images from the two high-resolution seismic lines taken by the *JOIDES Resolution* across Site 976 (Figs. 5, 6) and those from a multichannel seismic (MSC) composite-line (5 s, TWT penetration) located about 25 km northeast of Site 976, traversing the entire depocenter of the northern branch of the Western Alboran Basin (Fig. 7). Among several options, we chosen this MCS line to support our conclusion as ages and thickness of the lower sedimentary units in the basin are constrained from Alboran Alb-A1 well data. Figure 8 shows a basement contour map of the same depocenter, including the northwest slope of the Site 976 basement high.

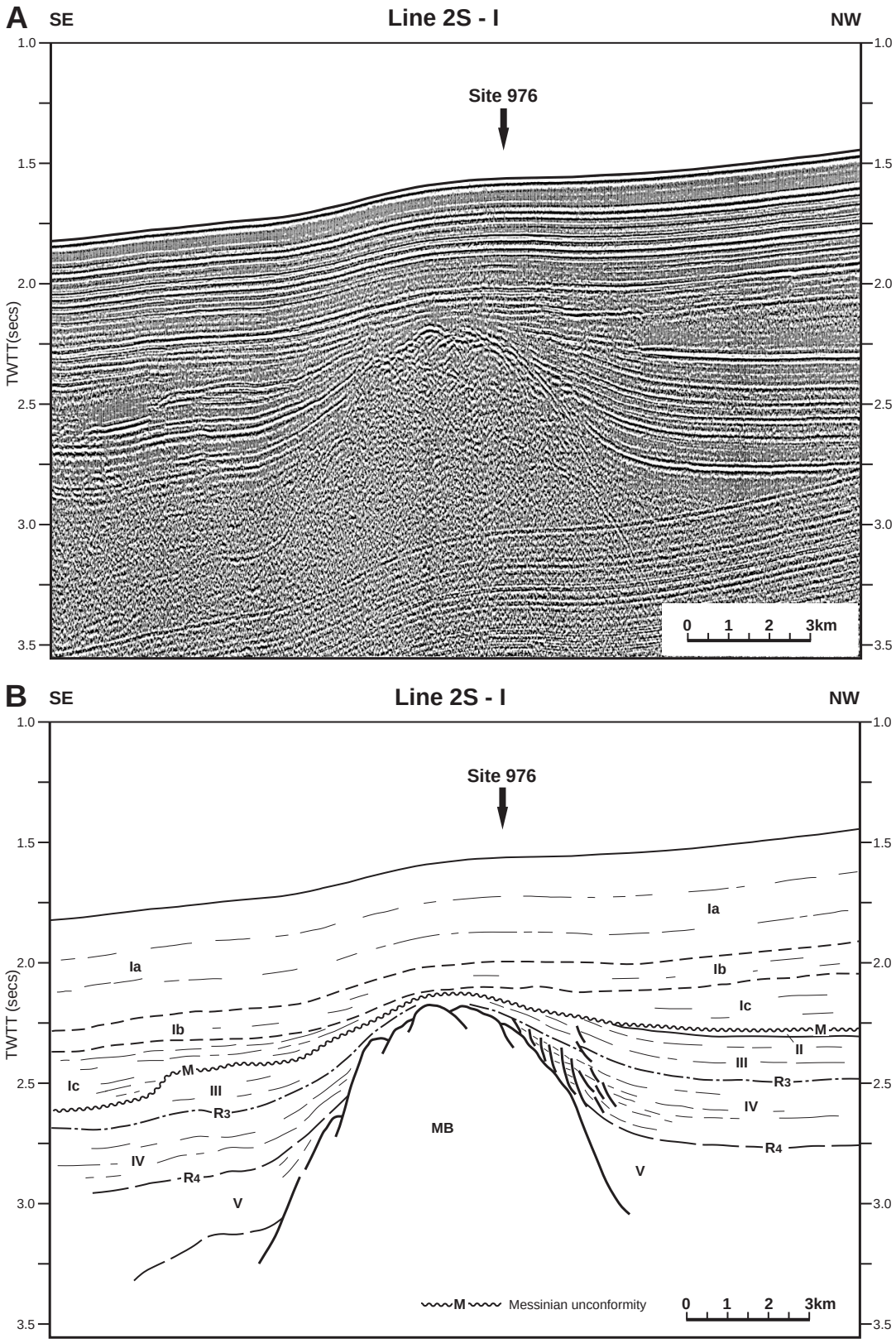

Figure 6. *JOIDES Resolution* seismic Line 2S-I (single channel) across Site 976. **A.** Original profile. **B.** Drawn interpretation of Line 2S-I based on Site 976 data (modified from Shipboard Scientific Party, 1996). Reflectors and lithoseismic units I–V from Comas et al. (1992). Reflectors correspond to major unconformities within sediments: R4 = middle Miocene, R3 = early Tortonian, M = Messinian "M" unconformity. Ia = Pleistocene, Ib and Ic = Pliocene sequences (Comas, Zahn, Klaus et al., 1996). MB = Metamorphic basement. Location of seismic line is shown in Figure 1.

Normal faulting bounding the basement high is apparent from seismic Line 2S-1 (Fig. 6), and from this image the structural high may be considered as a simple horst (Shipboard Scientific Party, 1996). However, as examined below, shallow faulting in the top of the high does not reveal its structural behavior.

Noteworthy structural features can be deduced from the high-resolution seismic picture in Figure 6. The top of the basement is very irregular, similar to the basement top imaged along the perpendicular seismic line 2S-II (Fig. 5). In places this morphology is clearly related to high-angle normal faulting, which is consistent with data from brittle deformation of the basement. Although no indication of emersion has been encountered in basement breccias, concurrent erosional topography, perhaps submarine, cannot be discounted given this widespread basement-top morphology. In the northwest flank, individual reflectors within middle Miocene sediments (Reflector R4 and those within seismic Unit IV; Fig. 6) are normal faulted, indicating that extension continued until this time (Shipboard Scientific Party, 1996). However, small reverse faults are seen in the same northwest flank affecting upper Miocene (Reflector R3 and those within seismic Unit III) deposits, as well as an anticline attitude of late Miocene to Pleistocene sediments (seismic Unit III/Tortonian to Subunit Ic) capping the basement. We believe these seismic data indicate that the basement high has also been restructured by compressional tectonics during the contractive reorganization of the Alboran Sea basin (Comas et al., 1992). In addition, the pre-early Pliocene (pre-Subunit Ic; Fig. 6) erosion of the Messinian Unit II just above the basement high and even some steep drag structures in reflectors from Subunit Ic (early Pliocene) near the basement hinge seem to point to post-Messinian folding superimposed on the extensional structures. Accordingly, we suggest that the influence of later compressional structures uplifting the basement must be considered for any reliable conclusion on the Miocene extensional uplift of this high.

Around Site 976, the basement high trends northeast-southwest, turning to northwest-southeast toward the south (Fig. 2). To the northwest, it limits a complex graben filled with up to 5–6 km of lower Miocene (late Aquitanian(?)–early Burdigalian, 20–19 Ma) to Pleistocene sequences (Fig. 7). The complex geometry of the basement top beneath the basin (Fig. 8) probably results from the interference of different surfaces formed largely by low-angle and high-angle normal faults, oblique-slip faults, and the tops of roll-over structures related to major extensional detachments (de la Linde et al., 1996).

The seismic section in Figure 7 shows the asymmetric character of the graben. The northern slope corresponds to a very low-angle faulted surface formed most likely by horsetail faults or a listric fan rooted on deeper listric detachment faults within the basement (ap-

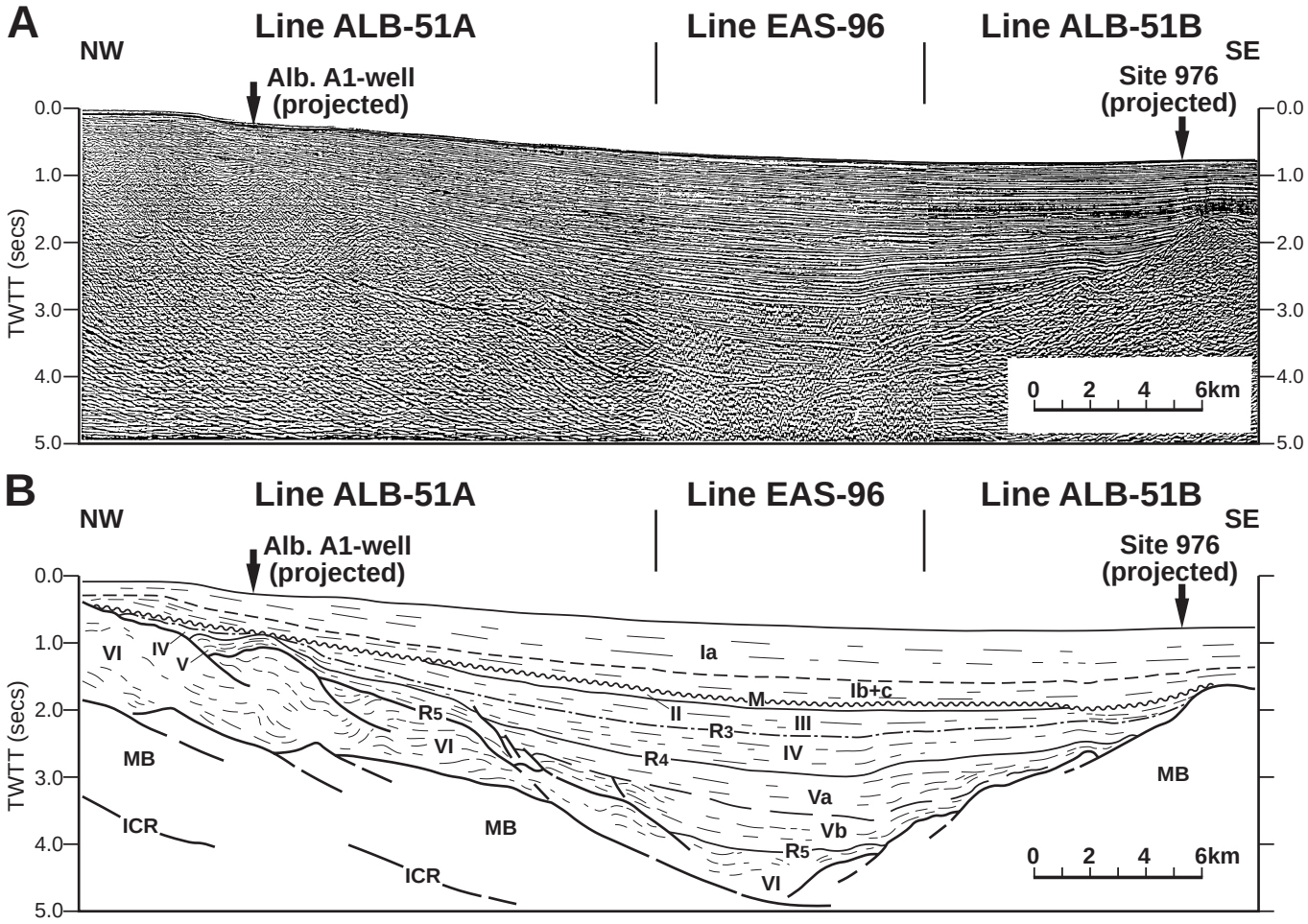

Figure 7. **A.** Composite profile from multichannel seismic reflection lines ALB-51A, EAS-96, and ALB-51B. **B.** Drawn interpretation of multichannel seismic reflection profile in (A). Reflectors and lithoseismic units I to V from Comas et al. (1992). Reflectors correspond to major unconformities within sediments: R5 = Burdigalian–Langhian, R4 = middle Miocene, R3 = early Tortonian, M = Messinian "M" unconformity (Comas, Zahn, Klaus, et al., 1996). Ia = Pleistocene, Ib and Ic = Pliocene. MB = metamorphic basement, ICR = Intracrustal reflectors. Location of seismic line is shown in Figure 2.

parent direction of extension toward the south-southeast). Individual reflectors (i.e., Reflectors R5 and R4) imaged in the northwest half of the MCS profile are tilted or rooted by low-angle normal faults within the sedimentary cover. This low-angle listric system is postdated by Reflector R3, which corresponds to about 11–10 Ma, intra-lower Tortonian sediments (Comas et al., 1992). In contrast, the steeper southern flank is cut by higher angle antithetic normal faults. From northwest to southeast, reflectors within the basin first diverge eastward and then progressively onlap or pinch out (or drag) against the basement (i.e., Reflectors R5, R4, and R3; Fig. 7). Reflector attitudes on the southern flank of the graben suggest that the basement scarpment developed from a sequence of faults, antithetic to the main low-angle listric fault, cutting back toward the top of the high, which developed from at least the Burdigalian–Langhian (Reflector R5, about 18–19 Ma), to the early Tortonian (Reflector R3, about 10–11 Ma). Given this set of structures in the graben, we interpret the basement high in this region as corresponding to a faulted rollover anticline in the hanging wall of a south-southeast–dipping major extensional detachment system. The rollover appears to be progressively extended by successive counter faults, therefore representing a central high (see Gibbs, 1984) in the Alboran Sea basin by the middle Miocene. The shallow crustal image presented here does not allow an interpretation of the extensional detachment system to deeper levels in the crust. However, single high-reflectivity reflections (intracrustal reflectors in Fig. 7) imaged at the western end of Figure 7 (at 3 to 5 s, TWT), seemingly ubiquitous in the Western Alboran Basin (Watts et al., 1993), suggest that the shallow extensional system is rooted in deeper and probably more complex intracrustal extensional detachments that caused major thinning of the Alboran Crustal Domain.

As similar asymmetric structures are observed the length of the graben southward to Site 976 (compare MCS profile in Fig. 7 with MCS profile ALB-39 in Fig. 3 of Shipboard Scientific Party, 1996), we determine that Site 976 was drilled in the same basement rollover as shown in Figure 7. The brittle deformation reported here may have formed largely because of middle Miocene antithetic counter faults and associated tensional conditions, developing near the top of a rollover structure. High-angle dip reported from the fault-gouge zone penetrated at Hole 976B (Fig. 5) as well as the steep main foliation in metamorphic rocks sampled at Site 976 may have originated from rotations of originally lower angle structures in this rollover.

Further implications from the above inference is that the exhumation of metamorphic basement rocks in the Western Alboran Basin took place up to the early Miocene (before deposition of seismic Unit VI; Fig. 7), and that the vertical relief of the basement high was uplifted later on and by steps, as the subsequent middle Miocene extension progressed in the basin. The basement high at Site 976 must have been exposed to the seafloor not only by the late Serravallian, as demonstrated by data from drilling, but has probably also been a submarine (or occasionally emergent?) high since the early Miocene.

CONCLUSIONS

The following conclusions can be drawn from the present work:

1. Holes 976B and 976E penetrated high-grade metamorphic rocks intersected by polymictic breccia and gouge intervals formed of high-angular and variable grain-sized clasts of near-

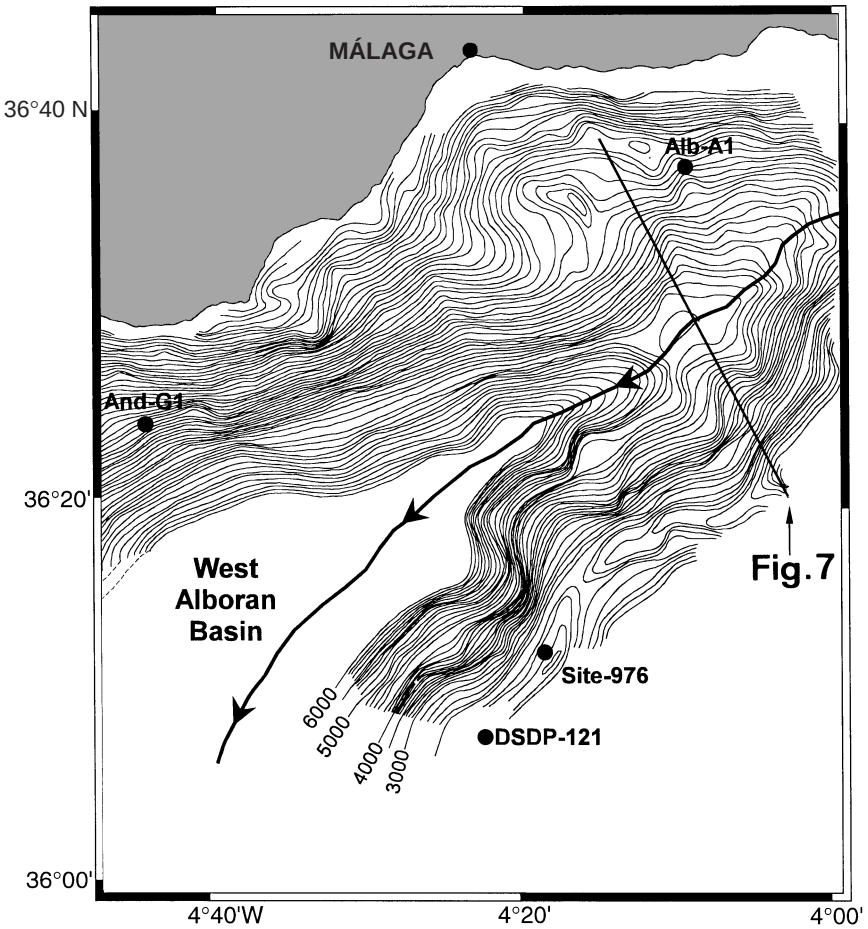

Figure 8. Contour map of basement depth in the northeastern branch of the Western Alboran Basin. Contour lines are every 100 ms (TWT). Note the complex fault-related morphology at the northwestern slope of the basement high on which Site 976 is located. Straight line shows the position of the multichannel seismic line in Figure 7. Alb-A1 and And-G1 = commercial boreholes. Bold line with arrows marks the northeastern end of the early Miocene main depocenter in the Western Alboran Basin; the whole path of this sedimentary depocenter is depicted in Figure 2.

by basement metamorphic lithologies. Fabrics at both meso- and microscopic scales indicate that breccias formed in situ by fracturing of the basement.

2. Cataclastic flow-structures and cataclastic fabrics common in both breccias and gouges allow us to consider these rocks are cataclasites. Fabrics reveal intense brittle frictional sliding and multi-stage fracture processes. Additionally, tensional fractures and internal splint-breakage textures in porphyroclasts indicates that dilation accompanied the brittle fracturing of the basement. Extensive replacive- and displacive-dolomite growing over cataclastic fabrics is interpreted to be formed as a result of pervasive fluid circulation in fracture zones. The occurrence of neptunian dikes (filled with Serravallian sediments) at the top of the basement prove that brittle deformation occurred at least partially in a submarine environment.
3. Intervals of breccia and gouges in Holes 976B and 976E mark zones of fault-related brittle deformation in the metamorphic basement. Logging data, together with macroscopic observations, reveal the occurrence of a thick fault zone with cataclastic rocks at 750–785 mbsf (Hole 976B) in the basement section. This fault zone coincides with a major change in basement lithology, which is richer in gneissic rocks downhole.
4. On the basis of seismic images from the basement high, the brittle deformation have been related to middle Miocene (before 12 Ma) faulting accounted by antithetic or counter faults in a rollover basement structure. High-angle dip of fault zones and main foliation in metamorphic rocks may have originated from rotations in this rollover. The basement high drilled at Site 976 is interpreted as a faulted central high from the early to middle Miocene extensional fault-system occurred in the Western Alboran basin.

ACKNOWLEDGMENTS

We are very grateful to the Shipboard Scientific Party, the ODP technicians, and the SEDCO drilling crew for their encouragement and effort when drilling basement at Site 976 during Leg 161. Comments from Kitty Milliken and Julia Morgan helped to improve this contribution. This work was funded by the CICYT (Spain) under Project AMB95-1557.

REFERENCES

Babaie, H.A., Babaie, A., and Hadizadeh, J., 1991. Initiation of cataclastic flow and development of cataclastic foliation in nonporous quartzites from a natural fault zone. *Tectonophysics*, 200:67–77.

Balanyá, J.C., García-Dueñas, V., Azañón, J.M., and Sánchez-Gómez, M., 1997. Alternating contractional and extensional events in he Alpujarride nappes of the Alboran Domain (Betics, Gibraltar Arc). *Tectonics*, 16:189–204.

Banda, E., Gallart, J., García-Dueñas, V., Danobeitia, J., and Makris, J., 1993. Lateral variation of the crust in the Iberia Peninsula: new evidence for the Betic Cordillera. *Tectonophysics*, 221:53–66.

Bellon, H., Bordet, P., and Montenat, C., 1983. Le magmatisme néogène des Cordillères bétiques (Espagne): cronologie et principaux caractères géochimiques. *Bull. Soc. Geol. Fr.*, Ser. 7, 25:205–218.

Bernoulli, D., and Jenkyns, H.C., 1974. Alpine, Mediterranean, and central Atlantic Mesozoic facies in relation to the early evolution of the Tethys. *Spec. Publ.— Soc. Econ. Paleontol. Mineral.*, 19:129–160.

Blenkinsop, T.G., and Sibson, R.H., 1992. Aseismic fracturing and cataclasis involving reaction softening within core material from the Cajon Pass Drill Hole. *J. Geophys. Res.*, 97:5135–5144.

Byerlee, J., 1990. Friction, overpressure, and fault normal compression. *Geophys. Res. Lett.*, 74:3821–3827.

Carter, N.L., Kronenberg, A.K., Ross, J.V., and Wiltschko, D.V., 1990. Controls of fluids on deformation of rocks. *In* Knipe, R.J., and Rutter, E.H. (Eds.), Deformation Mechanisms, Rheology and Tectonics. *Geol. Soc. Spec. Publ. London*, 54:1–13.

Chester, F.M., Friedman, M., and Logan, J.M., 1985. Foliated cataclasites. *Tectonophysics*, 111:139–146.

Comas, M.C., Dañobeitia, J.J., Alvarez Marrón, J., and Soto, J.I., 1995. Crustal reflections and structure in the Alboran Basin: preliminary results of the ESCI-Alboran Survey. *Rev. Soc. Geol. Esp.*, 8:76–88.

Comas, M.C., García-Dueñas, V., and Jurado, M.J., 1992. Neogene tectonic evolution of the Alboran Basin from MCS data. *Geo-Mar. Lett.*, 12:157–164.

Comas, M.C., Zahn, R., Klaus, A., et al., 1996. *Proc. ODP, Init. Repts.*, 161: College Station, TX (Ocean Drilling Program).

Crespo-Blanc, A., Orozco, M., and García-Dueñas, V., 1994. Extension versus compression during the Miocene tectonic evolution of the Betic Chain: late folding of normal fault systems. *Tectonics*, 13:78–88.

de la Linde, J., Comas, M.C., and Soto, J.I., 1996. Morfología del basamento en el nor-oeste del Mar de Alborán. *Geogaceta*, 20:355–358.

Evans, J.P., 1990. Textures, deformation mechanisms, and the role of fluids in the cataclastic deformation of granitic rocks. *In* Knipe, R.J., and Rutter, E.H. (Eds.), *Deformation Mechanisms, Rheology and Tectonics*. Geol. Soc. Spec. Publ. London, 54:29–39.

Gaines, A.M., 1980. Dolomitization kinetics: recent experimental studies. *In* Zenger, D.H., Dunham, J.B., and Ethington, R.L. (Eds.), *Concepts and Models of Dolomitization*. Spec. Publ.—Soc. Econ. Paleontol. Mineral., 21:81–86.

García-Dueñas, V., Balanyá, J.C., and Martínez-Martínez, J.M., 1992. Miocene extensional detachments in the outcropping basement of the northern Alboran basin (Betics) and their tectonic implications. *Geo-Mar. Lett.*, 12:88–95.

Gibbs, A.D., 1984. Structural evolution of extensional basin margins. *J. Geol. Soc. London*, 141:609–620.

Giermann, G., Pfannenstiel, M., and Wimmenauer, W., 1968. Relation entre morphologie, tectonique et volcanisme en mer d'Alboran (Mediterranée occidentale): resultats preliminaires de la campagne Jean-Charcot (1967). *C. R. Somm. Seances Soc. Geol. Fr.*, 4:116–118.

Hernandez, J., de Larouzière, F.D., Bolze, J., and Bordet, P., 1987. Le magmatisme néogène bético-rifain et le couloir de décrochement trans-Alboran. *Bull. Soc. Geol. Fr.*, 3:257–267.

House, W.M., and Gray, D.R., 1982. Cataclasites along the Saltville thrust, USA, and their implications for thrust-sheet emplacement. *J. Struct. Geol.*, 4:257–269.

Koestler, A.G., and Ehrmann, W.U., 1991. Description of brittle extensional features in chalk on the crest of a salt ridge (NW Germany). *In* Roberts, A.M., Yielding, G., and Freeman, B. (Eds.), *The Geometry of Normal Faults*. Geol. Soc. Spec. Publ. London, 56:113–123.

Malavieille, J., 1993. Late orogenic extension in mountain belts: insights from the Basin and Range and the late Paleozoic Variscan Belt. *Tectonics*, 12:1115–1130.

Martínez-Martínez, J.M., and Azañón, J.M., 1997. Mode of extensional tectonics in the southeastern betics (SE spain): implications for the tectonic evolution of the peri-alboran orogenic system. *Tectonics*, 16:205–225.

Monié, P., Torres-Roldán, R.L., and García-Casco, A., 1994. Cooling and exhumation of the western Betic Cordilleras, $^{40}Ar/^{39}Ar$ thermochronological constraints on a collapsed terrane. *Tectonophysics*, 238:353–379.

Platt, J.P., Soto, J.I., Comas, M.C., and Leg 161 Shipboard Scientists, 1996. Decompression and high-temperature–low-pressure metamorphism in the exhumed floor of an extensional basin, Alboran Sea, Western Mediterranean. *Geology*, 24:447–450.

Polyak, B.G., Fernàndez, M., Khutorsky, M.D., Soto, J.I., Basov, I.A., Comas, M.C., Khain, V.Y., Alonso, B., Agapova, G.V., Mazurova, I.S., Negredo, A., Tochitsky, V.O., de la Linde, J., Bogdanov, N.A., and Banda, E., 1996. Heat flow in the Alboran Sea (the Western Mediterranean). *Tectonophysics*, 263:191–218.

Ryan, W.B.F., Hsü, K.J., et al., 1973. *Init. Repts. DSDP*, 13 (Pts. 1 and 2): Washington (U.S. Govt. Printing Office).

Shipboard Scientific Party, 1996. Site 976. *In* Comas, M.C., Zahn, R., Klaus, A., et al., *Proc. ODP, Init. Repts.*, 161: College Station, TX (Ocean Drilling Program), 179–297.

Sibley, D.F., and Gregg, J.M., 1987. Classification of dolomite rock textures. *J. Sediment. Petrol.*, 57:967–975.

Sibley, D.F., Nordeng, S.H., and Borkowski, M., 1994. Dolomitization kinetics in hydrothermal boms and natural settings. *J. Sediment. Res.*, 3:630–637

Sibson, R.H., 1996. Structural permeability of fluid-driven fault-fracture meshes. *J. Struct. Geol.*, 18:1031–1042.

Tanaka, H., 1992. Cataclastic lineations. *J. Struct. Geol.*, 14:1239–1252.

Torné, M., and Banda, E., 1992. Crustal thinning from the Betic Cordillera to the Alboran Sea. *Geo-Mar. Lett.*, 12:76–81.
Twiss, R.J., and Moores, E.M., 1992. *Structural Geology:* New York (Freeman).
Watts, A.B., Platt, J.P., and Buhl, P., 1993. Tectonic evolution of the Alboran Sea Basin. *Basin Res.*, 5:153–177.
Wintsch, R.P., Christoffersen, R., and Kronenberg, A.K., 1995. Fluid-rock reaction weakening of fault zones. *J. Geophys. Res.*, 100:13021–13032.
Zeck, H.P., Monié, P., Villa, I.M., and Hansen, B.T., 1992. Very high rates of cooling and uplift in the Alpine belt of the Betic Cordilleras, southern Spain. *Geology*, 20:79–82.

Date of initial receipt: 16 May 1997
Date of acceptance: 19 December 1997
Ms 161SR-226

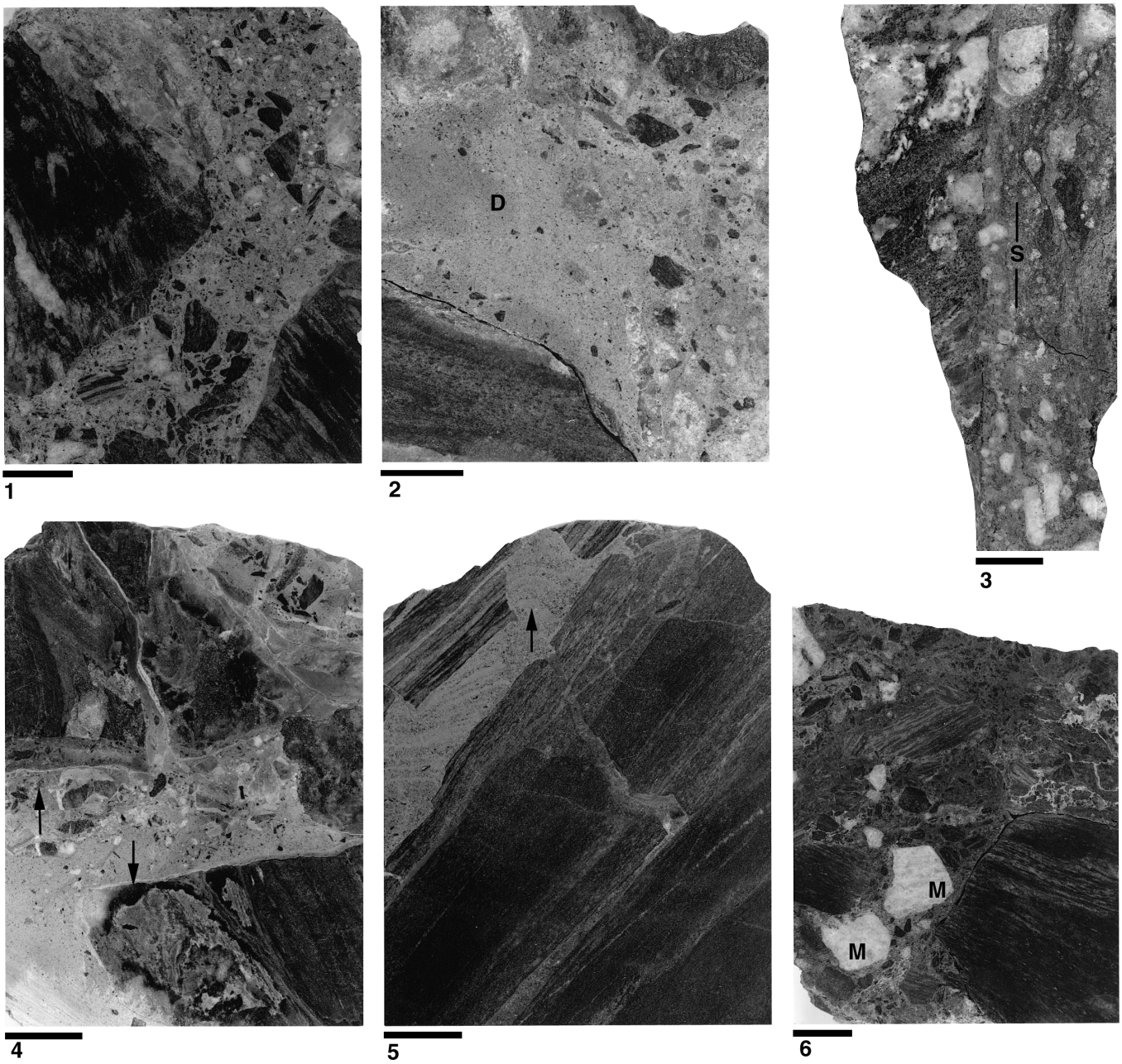

Plate 1. Hand-specimen photographs of representative breccia. In all figures, the scale bar is 1 cm, and the top of photographs is up-core. **1.** Sample 161-976B-75R-1, 64–73 cm. Unsorted cataclastic breccia with angular clasts of high-grade schist. Observe clasts broken from single porphyroclasts, within a light-colored groundmass or matrix that fills a major fracture between larger metamorphic porphyroclasts. **2.** Sample 161-976B-75R-1, 94–103 cm. Fine-grained breccia-groundmass and metamorphic porphyroclast in the left lower corner with dolomitic matrix (D) including foraminifer ghosts. **3.** Sample 161-976B-105R-1, 130–144 cm. Fault gouge (right side) with a clay-rich groundmass and a very noticeable cataclastic foliation (S). **4.** Sample 161-976E-17R-1, 119–126 cm. Dolomite-breccia similar to that shown in (2). Angular clasts are surrounded by light, narrow rims of nonplanar replacive dolomite (arrows). The breccia is cut by later, narrow white calcite veins. Note somewhat larger clasts concentrated on the top of the sediment-filled fracture. **5.** Sample 161-976E-21R-2, 48–55 cm. Open fractures fill with laminated particulate sediments, showing convex-upward geometries (arrow). Notice that fracture wall can be fitted together. **6.** Sample 161-976E-21R-2, 84–92 cm. Cataclastic cemented breccia with porphyroclasts of white marble (M) and schist.

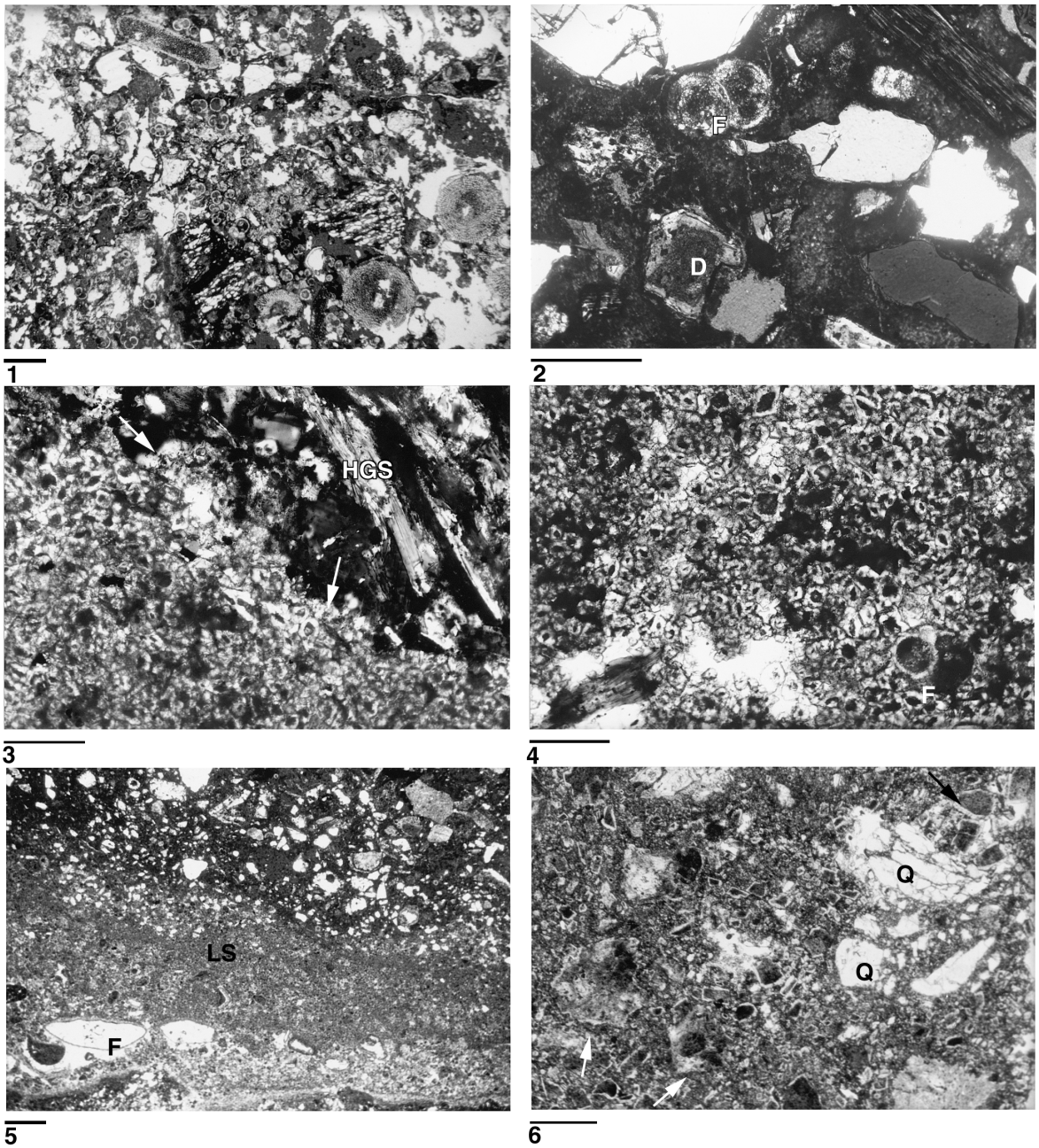

Plate 2. Thin-section photomicrographs of upper breccia intervals and overlying sediments from Holes 976B and 976E. **1.** Sample 161-976B-72X-1, 2–5 cm. Upper Serravallian, glauconite, foraminifer-rich, coarse lithic-sandstone. Crossed polars. Scale bar = 1 mm. **2.** Sample 161-976B-72X-2, 110–113 cm. Detail of similar cemented sandstone as in (1) showing a ghost of foraminifers (F) and euhedral dolomite (D) crystals in a dark clayey matrix. Crossed polars. Scale bar = 200 µm. **3.** Sample 161-976B-74R-1, 1–3 cm. nonplanar to planar replacive dolomite (RD) in breccia matrix. Note replacement (arrows) of schist (HGS) clasts by dolomite. Crossed polars. Scale bar = 100 µm. **4.** Sample 161-976B-74R-1, 1–3 cm. Detail of (1) showing two generations of replacive dolomite in breccia matrix. Note ghost of foraminifers (F) in the lower right corner. Light rims of dolomite darker grains are dolomite overgrowths. Plane light. Scale bar = 100 µm. **5.** Sample 161-976E-16R-1, 113–117 cm. Sediment-filled fissure in fine cataclastic breccia. Note large geopetal infill of larger foraminifers (F), passing upward to laminated internal sediments (LS). Plane light. Scale bar = 1 mm. **6.** Sample 161-976E-17R-2, 106–110 cm. Dolomite matrix, cataclastic breccia. Note light euhedral rims of second-generation dolomite bounding darker dolomite fragments (arrows). Note cataclastic breakage and cataclastic flow in quartzite clast (Q) at the right-hand side. Plane light. Scale bar = 500 µm.

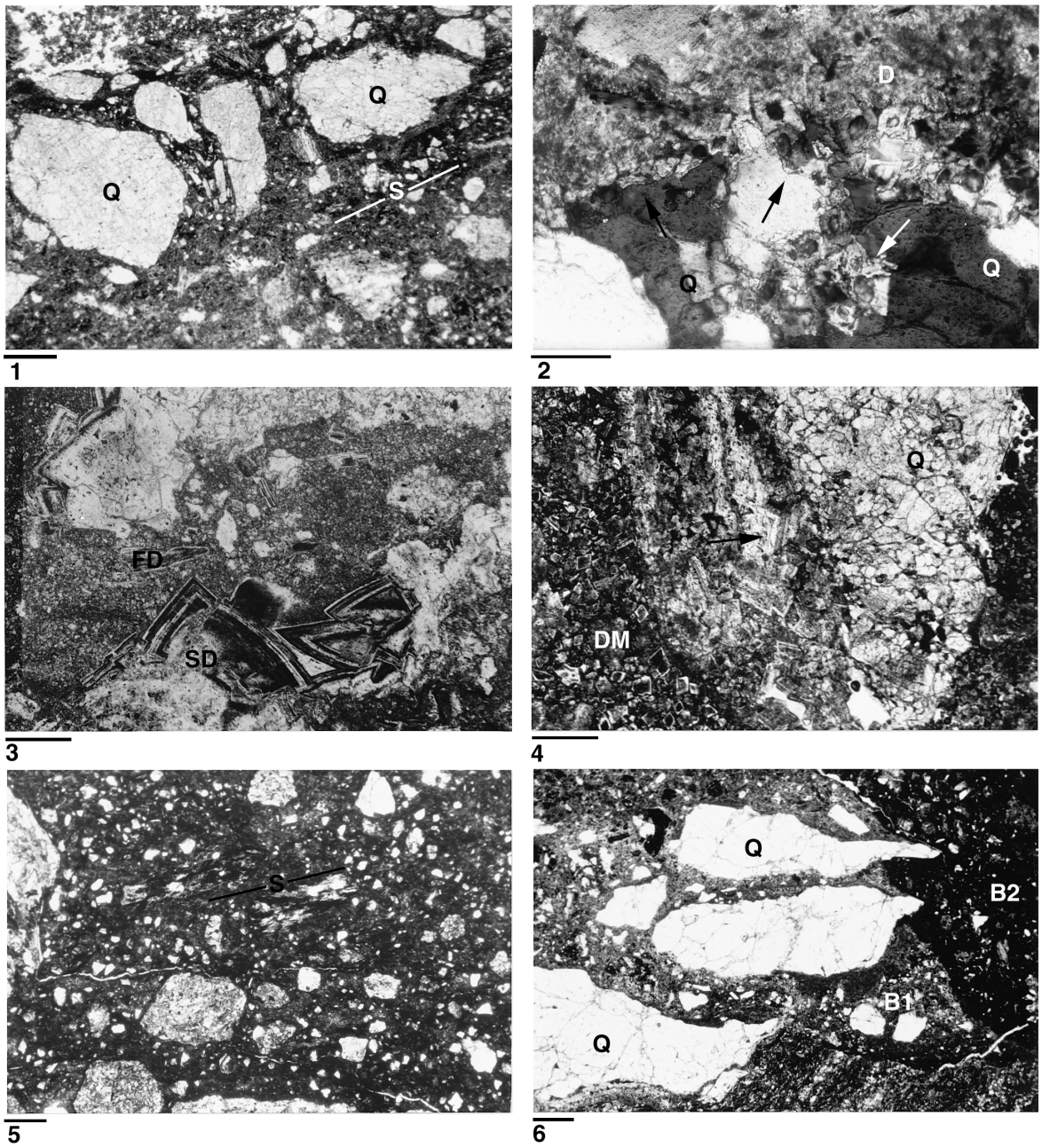

Plate 3. Thin-section photomicrographs of dolomite-cemented to clay-rich matrix cataclastic breccias from Holes 976B and 976E. **1.** Sample 161-976B-75R-1, 52–56 cm. Broken quartzite porphyroclast (Q) surrounded by vague cataclastic foliation (S). All of the finer matrix is replacive dolomite "cement." Note open crack in the clast filled by matrix. Plane light. Scale bar = 1 mm. **2.** Sample 161-976B-75R-1, 52–56 cm. Close-up of matrix in (1) showing planar (euhedral) to nonplanar dolomite (D). Dolomite rhombus growth over "cloudy" nonplanar dolomite. Note replacement of quartz grains (Q) by dolomite crystals (arrows). Crossed polars. Scale bar = 100 µm. **3.** Sample 161-976B-78R-1, 106–110 cm. Saddle dolomite cement (SD) and detrital dolomite filling a void in dolomite breccia. Note a fragment of saddle dolomite (FD) within the dolomite matrix filling the void and several zones of saddle dolomite growth. Crossed polars. Scale bar = 500 µm. **4.** Sample 161-976B-80R-1, 103–107 cm. Dolomite-matrix breccia. Note dolospar cement at the contact of quartzite clast (Q) and dolomitic matrix (DM). Note large euhedral crystal coarsening inward at the matrix/clast boundary (arrow). Plane light. Scale bar = 500 µm. **5.** Sample 161-976B-86R-2, 80–83 cm. Clay-matrix cataclastic breccias. Note cataclastic lineation and cataclastic flow (S) marked by alienation of smaller and elongated clasts. Plane light. Scale bar = 1 mm. **6.** Sample 161-976E-21R-2, 75–80 cm. Clay-matrix, cataclastic breccias. Note two generations of breccias (B1 and B2), corresponding to light and dark color in matrix, and broken quartzite porphyroclast (Q). Plane light. Scale bar = 1 mm.

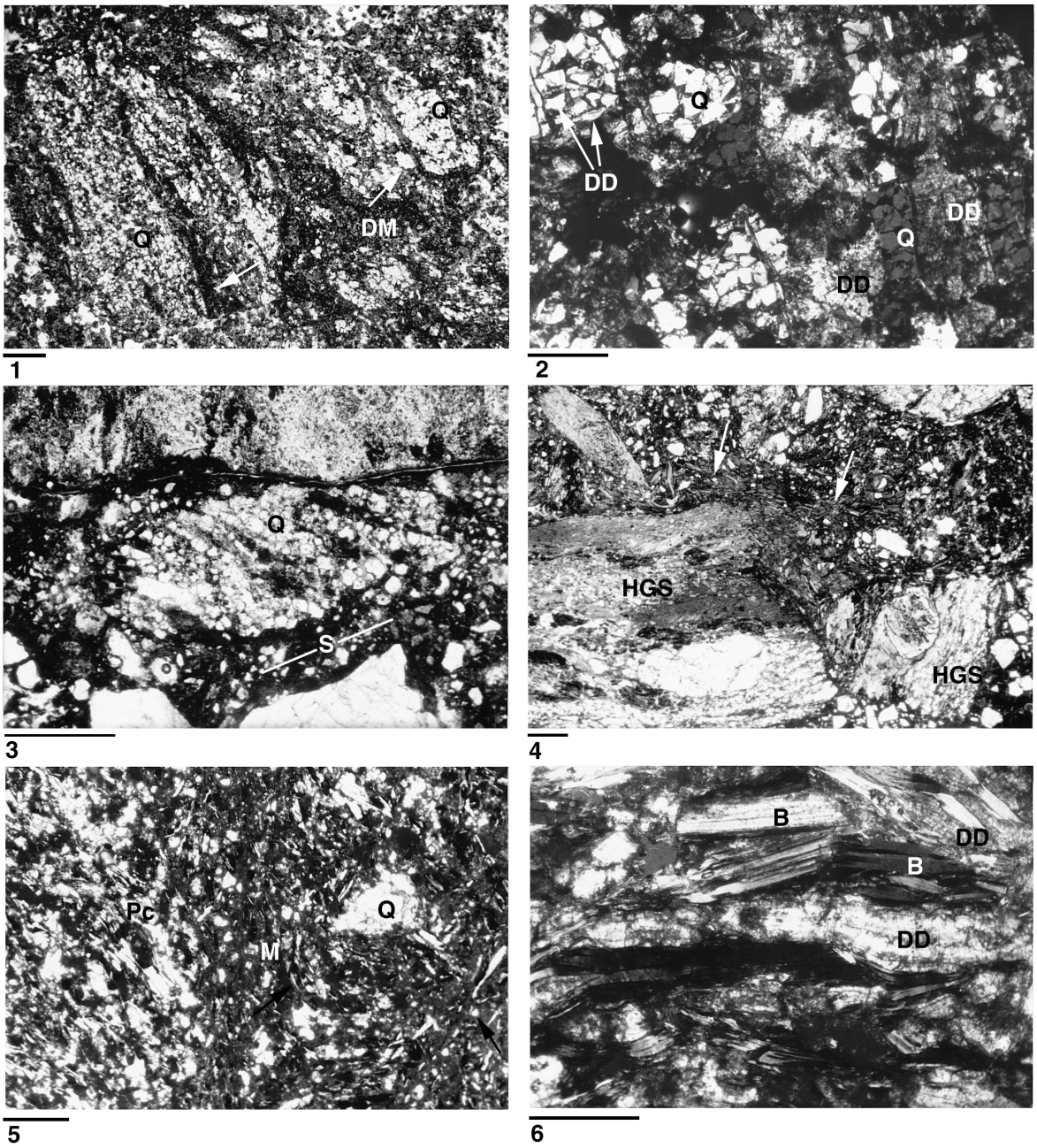

Plate 4. Thin-section photomicrographs of structures in clay-rich matrix cataclastic breccias. **1.** Sample 161-976B-80R-2, 1–8 cm. Breccia formed of splintered quartzite porphyroclasts (Q) in clayey dolomite-rich matrix (DM). Note widespread displacive-dolomite filling internal cracks (arrows) in porphyroclasts. Plane light. Scale bar = 1 mm. **2.** Sample 161-976B-80R-2, 1–8 cm. Detail of (1) showing inner intensive fracture in splintered quartz porphyroclasts (Q) and darker bladed dolomite veins (DD). Note that displacive-dolomite (DD) also occurs between quartz fragments in splintered grains. Crossed polars. Scale bar = 100 µm. **3.** Sample 161-976B-88R-1, 17–20 cm. Cataclastic breakage of a splintered quartzite clast (Q). Note cataclastic comminute grains and cataclastic flow (S). Tails of the clast indicating the sense of shear. Plane light. Scale bar = 200 µm. **4.** Sample 161-976B-91R-1, 44–47 cm. Intensive cataclastic breakage of a garnet-bearing schist porphyroclast. Note lack of displacement between the broken halves of porphyroclast (HGS) and pronounced cataclastic flow marked by alienation of micas (arrows). Plane light. Scale bar = 1 mm. **5.** Sample 161-976B-105R-1, 130–131 cm. High-turbulence cataclastic flow in breccia matrix, showing "whirlwind" arrangement of micas around a quartzite clast (Q). Note high-grade schist porphyroclast (Pc) at the left-hand side. Plane light.Scale bar = 500 µm. **6.** Sample 161-976B-106R-1, 62–66 cm. Plane light. Displacive dolomite (DD) in biotite grain (B). Scale bar = 200 µm.